Improved determination of the Boltzmann constant using a single, fixed-length cylindrical cavity

2013 Metrologia 50 417

(http://iopscience.iop.org/0026-1394/50/5/417)

Metrologia **50** (2013) 417–432 doi:10.1088/0026-1394/50/5/417

Improved determination of the Boltzmann constant using a single, fixed-length cylindrical cavity

H Lin[1], X J Feng[1], K A Gillis[2], M R Moldover[2], J T Zhang[1], J P Sun[1] and Y Y Duan[3]

[1] National Institute of Metrology, Beijing 100013, People's Republic of China
[2] National Institute of Standards and Technology, Gaithersburg, MD 20899-8360, USA
[3] Key Laboratory of Thermal Science and Power Engineering of MOE, Beijing; Key Laboratory for CO_2 Utilization and Reduction Technology, Tsinghua University, Beijing 100084, People's Republic of China

E-mail: zhangjint@nim.ac.cn

Received 18 April 2013, in final form 2 July 2013
Published 27 August 2013
Online at stacks.iop.org/Met/50/417

Abstract
We report improvements to our previous (Zhang *et al* 2011 *Int. J. Thermophys.* **32** 1297) determination of the Boltzmann constant k_B using a single 80 mm long cylindrical cavity. In this work, the shape of the gas-filled resonant cavity is closer to that of a perfect cylinder and the thermometry has been improved. We used two different grades of argon, each with measured relative isotopic abundances, and we used two different methods of supporting the resonator. The measurements with each gas and with each configuration were repeated several times for a total of 14 runs. We improved the analysis of the acoustic data by accounting for certain second-order perturbations to the frequencies from the thermo-viscous boundary layer. The weighted average of the data yielded $k_B = 1.380\,6476 \times 10^{-23}$ J K^{-1} with a relative standard uncertainty $u_r(k_B) = 3.7 \times 10^{-6}$. This result differs, fractionally, by $(-0.9 \pm 3.7) \times 10^{-6}$ from the value recommended by CODATA in 2010. In this work, the largest component of the relative uncertainty resulted from inconsistent values of k_B determined with the various acoustic modes; it is 2.9×10^{-6}. In our previous work, this component was 7.6×10^{-6}.

(Some figures may appear in colour only in the online journal)

1. Introduction

In 2005, *the Comité international des poids et mesures* (CIPM) recommended redefining the base units of the SI, including the kelvin, in terms of a set of fundamental constants [1]. The CIPM recommended that the kelvin be redefined in terms of the Boltzmann constant k_B. To provide continuity with the existing definition of the kelvin, the thermometry community is re-measuring k_B using several different methods. CODATA will weight all the measurements of k_B by their uncertainties to establish its most likely value. When the kelvin is redefined, the value of k_B will become the CODATA value with zero uncertainty and the temperature of the triple point of water T_{TPW} will remain 273.16 K; however, T_{TPW} will have the fractional uncertainty of the CODATA-weighted average of the measurements of k_B.

The Boltzmann constant k_B relates the thermodynamic temperature to thermal energy. Since the 1970s, the acoustic resonance method has been used to determine k_B [2–8], thermodynamic temperatures [9–15] and the thermophysical properties of gases. Determinations of k_B using acoustic resonators rely on two relationships. The first relationship, $(1/2)mv_{RMS}^2 = (3/2)k_BT$, connects the root-mean-square (RMS) velocity of an atom of mass m to its kinetic energy (hence to the thermodynamic temperature). The second relationship, $v_{RMS}^2 = (3/\gamma_0)c_0^2$, connects the RMS velocity to the zero-frequency speed of sound c_0 of the same gas and to the heat-capacity ratio $C_p^0/C_v^0 \equiv \gamma_0$ of the gas. For a monatomic gas γ_0 is exactly 5/3. Accordingly, the acoustic resonator method infers c_0 by combining measurements of the acoustic resonance frequencies of an argon-filled or helium-filled cavity at various pressures at T_{TPW} with appropriate dimensions of the

cavity. The measured frequencies are corrected for the thermal and viscous boundary layers where the gas contacts the walls of the cavity, imperfect accommodation of gas atoms with the walls, the imperfect shape of the cavity, motions of the cavity's walls and the effects of electro-acoustic transducers. The corrected frequencies for each mode are combined with that mode's eigenvalue and the cavity's dimensions to determine $c(p,T_{\mathrm{TPW}})$. Then, $c^2(p,T_{\mathrm{TPW}})$ is fitted to the acoustic virial equation to determine c_0 for the gas. Finally, the Boltzmann constant is obtained through the relation

$$k_{\mathrm{B}} = c_0^2 M/(T\gamma_0 N_{\mathrm{A}}), \tag{1}$$

where M is the average molar mass of the gas, as determined from chemical and isotopic analysis, and N_{A} is the Avogadro constant. The relative uncertainty of N_{A} is 3×10^{-8}, which is two orders of magnitude smaller than the uncertainty of k_{B} [16, 19]. Therefore, we consider N_{A} to be known.

For the highest possible accuracy, acoustic resonance measurements in dilute gases use non-degenerate modes, such as the radially symmetric modes of a spherical or quasi-spherical cavity and the longitudinal and radial modes of a cylindrical cavity. The radially symmetric modes of a spherical cavity have higher quality factors than the longitudinal modes of a cylindrical cavity of equal volume; therefore, spherical cavities are preferred [3]. We acknowledge that the two most important measurements of k_{B} using quasi-spherical cavities claim the low fractional standard uncertainties of 1.2×10^{-6} and 0.71×10^{-6} [4, 17].

In this work, we re-determine k_{B} using the non-degenerate longitudinal modes of a fixed-length cylindrical cavity. In doing this, we follow the recommendation of the Consultative Committee of Thermometry (CCT) that the redefinition of the kelvin should be based on three different methods of measuring k_{B}. We mention four differences between our method and previous work that used spherical or quasi-spherical cavities. (1) The longitudinal acoustic modes of fixed-length cylindrical cavities dissipate acoustic energy at the wall of the cavity through viscosity. This dissipation mechanism is not present for the radial acoustic modes in quasi-spherical cavities. Therefore, we test the understanding of acoustic resonances in a new regime. (2) The oscillations of the walls (the shell) of cylindrical and spherical cavities respond to the gas's oscillations in different patterns. For example, the non-degenerate longitudinal gas modes of the cylindrical cavities have either even or odd symmetry about the plane bisecting the cylinder's axis. In contrast, the $l = 1$ modes of a spherical cavity, which have odd symmetry about a bisecting plane, are degenerate; therefore, they are not used to determine k_{B}. (3) We used two-colour optical interferometry to measure the lengths of our cylindrical cavities. In contrast, the quasi-spherical-cavity method has used either pycnometry or microwave resonances to measure the volume of the cavity. (4) We used piezoelectric transducers located outside the cavity's wall to generate and detect acoustic signals. In contrast, small capacitive microphones embedded in the cavity's wall have been widely used with spherical cavities. The PZT detector has much larger capacitance than a capacitive microphone. The larger capacitance allowed us to connect the PZT to a remote amplifier with a coaxial cable. (In contrast, a small, capacitive microphone requires either a nearby preamplifier or a tri-axial cable with a driven shield connecting the capacitor to a remote preamplifier.)

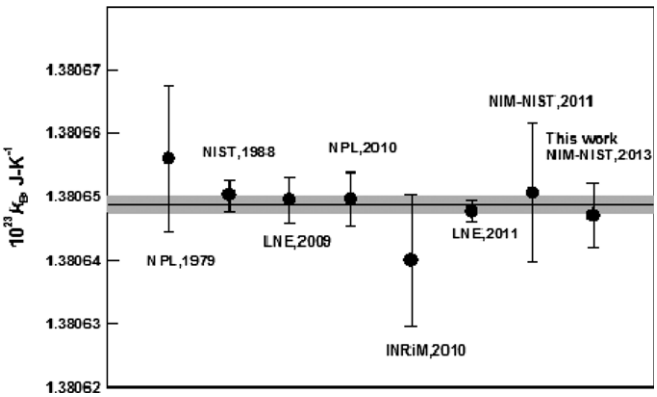

Figure 1. Comparison of the determination of k_{B} using acoustic thermometry with the CODATA 2010 recommended value [19].

In our previous, preliminary re-determination of k_{B}, we used a single, 130 mm long cylindrical cavity [8] and fitted the apparent speed of sound $c^2(p)$ for each of the six modes to zero pressure to get six values of c_0^2. The inconsistency among the six values of c_0^2 was the largest contribution to uncertainty of our preliminary value of k_{B}. Since then, we have studied five cylindrical, fixed-length cavities [18] and found that an 80 mm long cavity was the best of the five. In this paper, we present a new determination of k_{B} based on the average of the fourteen measurement runs using four modes of an improved 80 mm long cavity. Our principal result is $k_{\mathrm{B}} = (1.380\,6476 \pm 0.000\,0051) \times 10^{-23}\,\mathrm{J\,K^{-1}}$. This new value of k_{B} has a relative standard uncertainty $u_{\mathrm{r}}(k_{\mathrm{B}}) = 3.7 \times 10^{-6}$; it differs, fractionally, by -0.9×10^{-6} from the value recommended by CODATA in 2010 [19]. (Unless otherwise stated, all uncertainties in this paper are standard uncertainties with coverage factor $k = 1$ corresponding to 68% confidence level.) Figure 1 displays a comparison of the current values of k_{B} with those determined by the spherical and the quasi-spherical cavities [3–8]. Our new determination of k_{B} is consistent with our previous determination of k_{B} using the 130 mm long cylindrical cavity; however, the uncertainty of the present result is smaller by a factor of 2.1.

2. Fundamentals of the measurement

The unperturbed resonant frequencies f_l^0 of the longitudinal acoustic modes $(l\,0\,0)$ of a gas-filled, geometrically perfect, rigid, perfectly thermally insulating, cylindrical cavity are determined by the speed of sound in the gas c and the length L of the cavity by the formula

$$f_l^0 = lc/(2L), \tag{2}$$

where $l = 1, 2, \ldots$ is the longitudinal mode index (the eigenvalue). (Because this work uses only purely longitudinal modes, we identify these modes using only the longitudinal index l in subscripts. Other modes are designated by the

complete triplet of indices.) We combine equations (1) and (2) to relate k_B to the acoustic resonance frequencies of an idealized, gas-filled cavity:

$$k_B = \left(\frac{2 f_l^0 L}{l}\right)^2 \frac{M}{T \gamma_0 N_A}. \quad (3)$$

Our cavity had a nominal radius $a \approx 40$ mm and a nominal length of 80 mm. We used the modes $l = 2$, 3, 4 and 5 which have resonance frequencies spanning the range from 3.8 kHz to 9.6 kHz. We did not include data for the $l = 1$ mode in the analysis because excessive noise in the transducer signal and line-shape distortion, due in part to the mode's low Q, resulted in poor quality fits that did not improve with more averaging.

Practical cavities have an imperfect geometry. The duct that admits gas into the cavity is an opening in the wall of the cylindrical shell. The cylindrical shell and the end-plates are not rigid; therefore, they deform when they are bolted together and they deform elastically in response to the acoustic pressure oscillations in the gas. The oscillating gas forms a thermal and a viscous boundary layer on the walls of the shell. The end-plates have thin, machined diaphragms that separate the PZT transducers from the gas; these diaphragms present a lower impedance to the gas than the surrounding surfaces of the shell. The transducers generate heat when operating. All these complications perturb acoustic resonance frequencies from their ideal values f_l^0. By design, we minimized these perturbations; however, we must still correct the measured frequencies for these perturbations before using equation (3). In our previous papers [8, 20–22] we modelled these perturbations; here, we list them in sections 4.5.3 and 4.5.4.

3. Experimental setup and cylindrical cavity

Figure 2 is an overview of the apparatus. The experimental setup retained the main features that we described in detail in [8]. Here, we describe only a few key features and the changes that we made.

As in our previous work [8], the cylindrical cavity was formed by clamping two fused-silica end-plates to the ends of a thick-walled, steel 'tube' (see figure 3). The nominal length and the nominal diameter of the cylindrical cavity were 80 mm and the outer diameter of the cylindrical tube was 160 mm. The tube was made of bearing steel that had a Young's modulus of 210 GPa, a Poisson's ratio of 0.29 and a density of 7800 kg m^{-3}.

Because one of the 20 mm thick end-plates used in our previous work had cracked, we used new end-plates that were 15 mm thick and had a diameter of 108 mm. To reduce the stress on the new end-plates, they were clamped to the cylindrical shell with fewer M8 bolts (16 instead of 20) and with smaller torques (3.5 N m instead of 4.5 N m). The end-plates were fabricated from optical-quality, fused silica with a Young's modulus of 73 GPa, a Poisson's ratio of 0.17 and a density of 2210 kg m^{-3}. The inner surface of each end-plate was coated with a partially reflecting metallic film [8, 18].

As in our previous work, a blind hole was ground out of the outside-facing surface of each end-plate, leaving a silica diaphragm 0.25 mm to 0.30 mm thick, which was flush with the inside surface, thereby preserving the cylindrical shape of the cavity. The PZT transducers used in this work were the same type and size used in [8]. Epoxy was used to cement a PZT transducer to the outside surface of each diaphragm.

We used a single, small tube (fill duct) to measure and change the pressure of argon gas in the resonator, as in our previous work. The acoustic measurements were performed with a static charge of argon gas. This design minimized the perturbations to the shape of the cavity and the accompanying shifts in the resonance frequencies for which corrections must be made.

The fill duct of the present resonator was made of three sections of cylindrical, electro-polished, stainless-steel tubing. The section that opened into the cavity had a length of 802 mm and an inside diameter (ID) of 1.03 mm. (In our previous work, this section had an ID of 2.13 mm.) The second section had a 2.13 mm ID and was 100 mm long. It connected to a larger duct (4.57 mm ID and 2000 mm long) which terminated in a tee. One arm of the tee led to a valve that connected the duct to the gas manifold. The other arm of the tee led to a similar three-section duct that terminated at another cavity resonator with an ID of 80 mm and a length of 160 mm. (We do not discuss the second cavity in this work.) We calculated the acoustic admittance of the duct using a waveguide model [22]. The model showed that the admittance of the valve and the duct leading to the second cavity had a negligible effect on the calculated perturbations.

The new fill duct was shrunk-fit inside a mating hole in the steel tube near one end-plate (see figure 3). In our previous work (figure 1 of [8]), the fill duct entered the cavity midway between the end-plates. After the fill duct was installed, it extended into the cavity. This extension and the inner surface of the cavity were simultaneously ground until the open end of the duct was flush with the inner surface of the tube. The assembly by shrink-fitting followed by grinding avoided the annular slit between the duct and the wall of the cavity that was present in our previous work. Therefore, the new duct generates smaller, more accurately modelled perturbations to the resonance frequencies than the previous one.

We made only minor changes to the manifold that supplied gas to the cavity. The manifold had been assembled using all-metal connectors and valves with bellows stem seals. All of the junctions and the valves were checked for leaks at 1 MPa. We discovered that the getter that was located immediately upstream from the fill duct did not remove all the nitrogen from the argon. Therefore, we replaced the Entegris[4] model CE2500KFI4R getter with an SAES[4] Model GC50 getter.

The manifold was wrapped with heating tapes so that it could be baked out to remove adsorbed gases. Prior to baking, the SAES getter was preheated for 2 h to reach its operating temperature of 400 °C and it was maintained at 400 °C throughout the bake-out. The bake-out lasted more

[4] In order to describe materials and procedures adequately, it is occasionally necessary to identify commercial products by manufacturer's name or label. In no instance does such identification imply endorsement by the National Metrology Institute or the National Institute of Standards and Technology or Tsinghua University, nor does it imply that the particular product or equipment is necessarily the best available for the purpose.

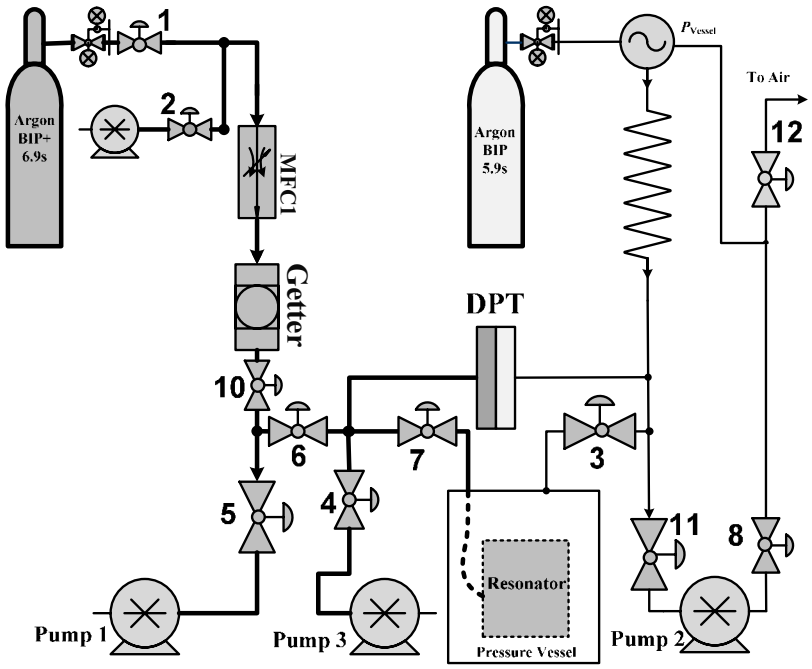

Figure 2. Sketch of the gas handling system. DPT denotes the differential pressure gauge and MFC1 denotes the mass flow controller.

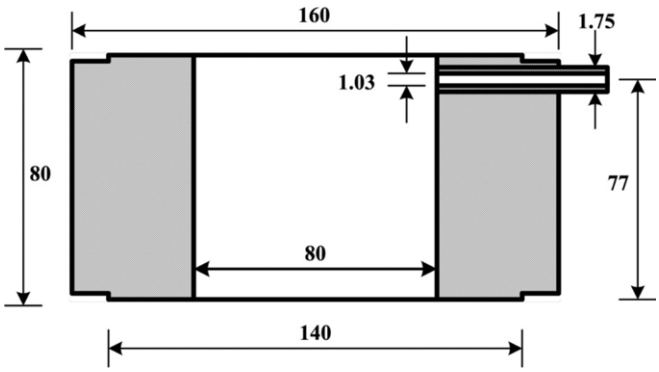

Figure 3. Schematic (not to scale) sketch of the cylindrical shell and the duct (all dimensions are in millimetres).

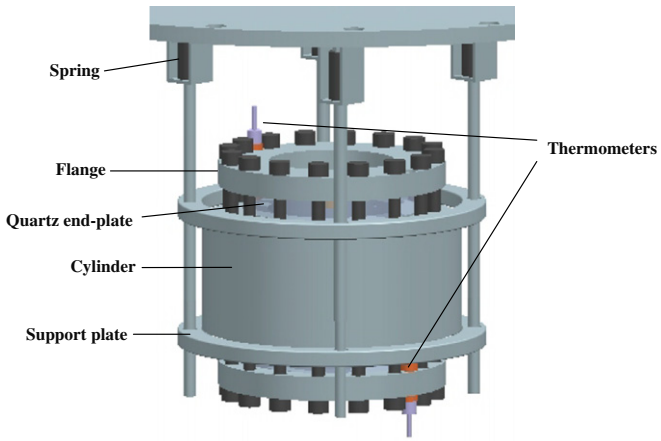

Figure 4. Cylindrical cavity assembly.

than 24 h. During the bake-out, the manifold was maintained at 100 °C while it was alternately evacuated and purged with pure argon. (The resonator was maintained at room temperature inside its thermostat.) The bake-out was repeated before starting each test run.

The temperature of the resonator was measured using two capsule-type standard platinum resistance thermometers (Hart 5686), each with a diameter of 5.5 mm and a sensing length of 30 mm. The thermometers were enclosed in metal sleeves that we describe in section 4.3. Figure 4 shows the locations of the thermometer wells in the assembled cylindrical resonator. We used an ASL F900 bridge and a 100 Ω standard resistor (Tinsley 5685A) to measure the resistance ratios of the thermometers. The thermostat maintained the resonator's temperature constant to within ±0.1 mK for 24 h.

The PZT sound generator was driven by a sinusoidal voltage generated by an Agilent 33220A waveform generator that was locked to a 10 MHz standard signal derived from a GPS clock. A frequency counter (Agilent 53131A) monitored the signal frequency from the waveform generator. The counter verified that the frequency stability was better than 0.05×10^{-6} during the measurement of a single mode. The signal from the PZT detector was measured with a two-phase lock-in amplifier (Stanford Research SR830) locked to the driving voltage.

An absolute pressure gauge (Ruska 7250 xi, 0 kPa to 600 kPa) controlled the argon gas pressure inside the pressure vessel at 200 Pa to 300 Pa below the pressure inside the cylindrical cavity. The mating surfaces of the end-plates and the cylinder were sufficiently flat that leakage of pure argon gas from the cavity into the pressure vessel was negligible. The overpressure in the cavity ensured that the argon inside the cavity would not be contaminated by outgassing from the transducers, epoxy, wire insulation, etc in the pressure vessel. A differential pressure gauge (MKS

Table 1. Properties of the three measurement cases.

Case	Gas	Number of modes	Number of runs	Number of measurements	Number of averaged measurements	Support	End-plates
I	BIP+	4	4	755	51	Free	Set 1
II	BIP+	4	6	1018	45	Clamped	Set 2
III	BIP	3	4	998	36	Clamped	Set 2

Baratron 616A, 100 Torr) (1 Torr $\equiv$ 133.32 Pa) measured the pressure difference between the cavity and the pressure vessel. The metal diaphragm of the differential pressure gauge isolated the cavity from the rest of the gas manifold. The absolute pressure gauge and the differential pressure gauge were calibrated by the National Institute of Metrology (NIM), China. The pressure uncertainty was estimated to be less than 20 Pa. The pressure uncertainty contributes no more than 0.05×10^{-6} to the uncertainty in k_B.

4. Measurements

4.1. Acoustic measurements: three cases

The procedures for the acoustic measurements were similar to those used during our preliminary determination of k_B [8]. However, to search for problems related to the mounting of the resonator, the mounting of the end-plates and the analysis of argon, we divided the measurement runs into three cases that are summarized in table 1.

During case I, the lower end of the resonator rested on a support plate. As shown in figure 4, the support plate hung from thin rods supported by springs. This compliant support allowed the resonator to respond as a nearly free body to the gas oscillations within it. (In our previous work, the resonator was tightly clamped to a rotational stage, which itself was clamped to the pressure vessel.) After completing the case I runs, the top and bottom end-plates were interchanged, and the resonator was replaced on the support plate and nuts were tightened on the threaded rods above the top of the resonator. Thus, the rods clamped the ends of the resonator together. This 'clamped' configuration was used for both cases II and III. As indicated in table 1, 'BIP Plus' argon supplied by Air Products was used during both cases I and II. As shown in figure 5, the values of k_B deduced from cases I and II were mode-dependent; however, they were mutually consistent. The five mode-by-mode differences yield $(k_B)_{\text{case II}} - (k_B)_{\text{case I}} = (0.54 \pm 0.41) \times 10^{-6} k_B$ where the uncertainty is the standard deviation of the differences between the circles and the squares in figure 5. (At the end of this section, we discuss the distinction between (4 0 0)*a* and (4 0 0)*b*.). We conclude that changing the method of support and interchanging end-plates did not change the value of k_B, within the small uncertainty of the comparison.

Between cases II and III, we changed the test gas from 'BIP Plus' argon to 'BIP' argon. The three values of k_B from cases II and III yield the average difference $(k_B)_{\text{case III}} - (k_B)_{\text{case II}} = (-2.85 \pm 0.50) \times 10^{-6} k_B$. This difference is 2.1 times the fractional standard uncertainty for determining the mole fraction average atomic mass $u_r(M)$ of each test gas (table 8)

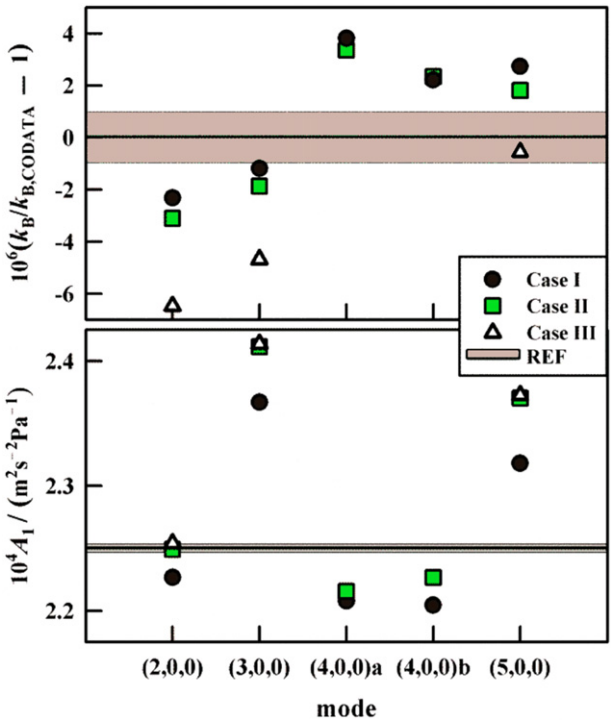

Figure 5. Top: values of the Boltzmann constant k_B determined using each of modes (2 0 0), (3 0 0), (4 0 0) and (5 0 0). Bottom: values of the acoustic slopes A_1 determined with the same modes. The grey band denotes reference values and their uncertainties. For reference values, we took k_B from CODATA 2010 [19] and A_1 from [3]. The type-A uncertainties from fitting the frequency data are comparable to the sizes of the plotted points. The distinction between (4 0 0)*a* and (4 0 0)*b* is discussed in section 4.1.

and 1.5 times $2^{1/2} u_r(M)$, which is the fractional standard uncertainty of the difference between two values of M. We conclude that the acoustic measurements are in reasonable agreement with the values of M and $u_r(M)$ that were estimated from independent gas analyses.

The 'BIP' argon for case III came from the same container that we used during our previous measurements with a 130 mm long cavity [8]. A sample drawn from this container had been analysed by the Center for Gas Metrology, Korea Institute of Standards and Science (KRISS), for chemical impurities and for relative abundances of the isotopes ^{36}Ar, ^{38}Ar and ^{40}Ar [8].

Case I was composed of four runs; that is, a quasi-isotherm near T_{TPW} was measured four times in succession. During each run, the resonance frequencies and half-widths were measured at six pressures. For half the runs, the pressures decreased from 550 kPa to 50 kPa in steps of 100 kPa. For the other half, the pressures decreased from 500 kPa to 100 kPa in steps of 100 kPa and additional measurements were made at 70 kPa. At

each pressure, the frequency and half-width of the longitudinal modes (2 0 0), (3 0 0), (4 0 0) and (5 0 0) were determined 8 to 12 times. The effects on resonance frequencies and half-widths due to known perturbations (sections 4.5.3 and 4.5.4) were calculated and used to correct the measurements. An inspection of the corrected frequency data showed that some unknown event occurred between 21 January 2012 and 24 January 2012 that separated the case I data for the (4 0 0) mode into two repeatable groups. For our analysis, we divided the (4 0 0) data into two groups before averaging: group *a* comprised the data acquired through 21 January 2012; group *b* comprised the data acquired after 24 January 2012. Averaging the corrected data at the same pressure for each mode reduced the number of data points for all the modes from 755 to 51.

Case II was composed of six runs. As in case I, the data for the (4 0 0) mode were separated into two groups: group *b* comprised the data acquired before 11 March 2012; group *a* comprised the data acquired after 11 March 2012. (This labelling suggests that the second unknown event restored the resonator to its initial condition. Our results are consistent with this assumption; however, our result for k_B is independent of the assumption.) Averaging the corrected case II data reduced the number of data points from 1018 to 45.

Case III was composed of four runs. For all these runs, the excess half-widths for the (4 0 0) mode were scattered with values 3 to 5 times larger than the half-widths for the other modes and some half-widths were negative. The excess half-widths did not have an obvious run dependence. Also, the scatter of the frequency measurements for the (4 0 0) mode was much larger than for the other modes. For these reasons, we did not use the (4 0 0) data for case III. Averaging the data for the (2 0 0), (3 0 0) and (5 0 0) modes reduced the number of data points to 36.

After completing the measurements for cases I, II and III, we disassembled the resonator. We discovered a crack in one of the quartz diaphragms that separated the cavity from a PZT transducer. We do not know whether this crack is connected with the anomalous behaviour of the (4 0 0) mode.

4.2. Measuring the length of the cavity

As in our previous work [8], the cylindrical cavity was defined by bolting two end-plates of optical-quality fused silica glass to a steel 'tube' to form the resonator. As in our previous paper [8], we measured the length of the cylindrical cavity using two-colour interferometry. Again, we used two lasers with nominal wavelengths 633 nm and 543 nm. Both lasers had beam diameters of approximately 1 mm and a fractional wavelength stability better than 2×10^{-8}.

The inner surface of each end-plate was coated with a semi-transparent, metallic film that increased its optical reflectivity while allowing the laser beams to penetrate the end-plates into the cavity. Because the end-plates were not exactly parallel, the laser beams formed two sets of equal-inclination interference patterns between the partially reflecting films. From measurements of the fractional fringes, we determined the optical length between the windows modulo 0.96 µm. In our previous study [8], we determined the required multiple

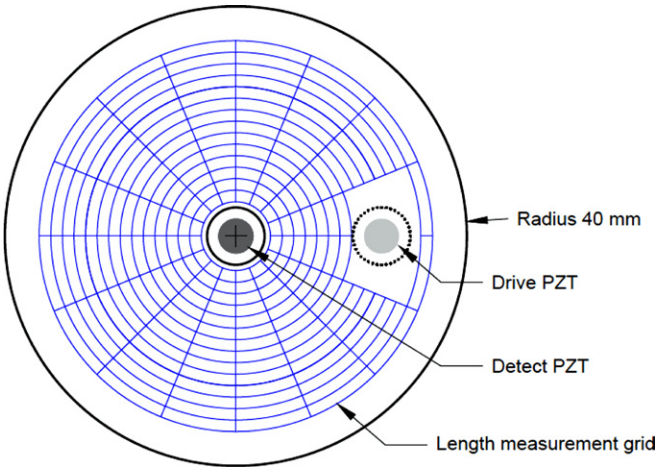

Figure 6. Grid of locations of length measurements.

of 0.96 µm by measuring the cavity's length with a coordinate measuring machine at ambient temperature and monitoring the thermal contraction of the cavity as it cooled to T_{TPW}. For this work, this time-consuming procedure was not necessary. Instead, we estimated the length of the cavity at T_{TPW} from the resonance frequencies of the longitudinal acoustic modes when the cavity was filled with pure argon. This estimate must have a fractional uncertainty less than 0.96 µm/(80 mm) $= 12 \times 10^{-6}$ to determine the correct multiple of 0.96 µm. In this work, the values of the length of the cavity deduced from various acoustic modes spanned the fractional interval $\pm 1.74 \times 10^{-6}$ which is accurate enough to select the correct multiple of 0.96 µm. Then, the two-colour interferometry refined the length estimate to achieve a length uncertainty of the order of 20 nm.

We conducted a two-colour interferometric measurement after completing the acoustic measurements at each pressure. It took several seconds to record the interference patterns. During and immediately following this short interval, the thermometers embedded in the metal wall of the cavity indicated a temperature increase of approximately 0.1 mK, which contributed a negligible uncertainty to the length measurement.

Because the two-colour length measurements were made at T_{TPW}, they accounted for any temperature-dependent deformation of the end-plates. In the current study, the shape of the end-plates was determined from the variation of the 633 nm interference patterns on a grid of 'spots' on the end-plates. As shown in figure 6, the grid was defined by the intersections of 16 radial lines with 15 equally spaced circles. We assumed that the shape of each end-plate was a quadratic function of the radius $L(r)$. Then, we computed the average length of the cavity $\langle L \rangle$ using equation (4), where the parameters a_i, b_i and c_i for the length $L_i(r)$ were fitted to the measurements on the grid.

$$\langle L \rangle = \frac{1}{8a^2} \sum_{i=1}^{16} \int_0^a r L_i(r)\, \mathrm{d}r, \tag{4}$$

$$L_i(r) = a_i r^2 + b_i r + c_i. \tag{5}$$

Table 2. Dimensions of the resonator.

Quantity	Symbol	Value/cm
Cavity radius	a	3.995 880
Cavity length		
Case I	L	7.996 166(4)
Cases II and III	L	7.996 086(4)
Shell thickness	h	4.0
End-plate radius	a_p	5.4
End-plate thickness	t_p	1.5
Diaphragm radius	a_d	0.5
Diaphragm thickness	t_d	0.025

The standard deviation of the values of $L_i(r)$ from the fitted curves was 43 nm; this is a contribution to the uncertainty of the average optical length of the cylinder. The curved end-plates perturb the frequencies of the $(l\,0\,0)$ modes; however, the first-order frequency shifts vanish for volume-preserving shape perturbations [23]. Thus, $\langle L\rangle$ using equation (4) is the appropriate average length for computing the frequencies of the $(l\,0\,0)$ modes.

As in our previous study, the resonator was installed in a pressure vessel filled with argon. The pressure inside the cavity was always 200 Pa to 300 Pa higher than the pressure outside the resonator, while the argon pressure within the cavity ranged 50 kPa to 550 kPa during the acoustic measurements. Thus, the resonator was subjected to significant hydrostatic pressures. The hydrostatic pressure at 50 kPa decreased the cavity's length by a fraction 1×10^{-7}; at 550 kPa the decrease was, fractionally, 9×10^{-7}. At zero pressure, the length of the cavity was 79.961 68 mm for case I with an uncertainty of 20 nm from two-colour interferometry. For cases II and III, the length was 79.960 88 mm with an uncertainty of 23 nm from interferometry. The larger length uncertainty contributed a fraction 0.58×10^{-6} to the uncertainty budget for the determination of k_B. For calculating the two-laser interference patterns, we relied on the accurate values of the refractivity of pure argon at 633 nm and 543 nm published in [24–28].

The inside surface of each end-plate had a partially reflective metallic coating protected by a dielectric overlayer. The manufacturer of the end-plates estimated that the thickness of each coating plus overlayer was between 5 nm and 20 nm. We do not know exactly how far the laser beams penetrated into the metallic coatings [29]; we estimated that the optical length of the cavity was 40 nm longer than the acoustic length. When calculating the speed of sound, we reduced the optical length by a fraction of 0.50×10^{-6} and added 1/2 of this value to the uncertainty of the acoustic length. From equation (3), k_B is proportional to the square of the cavity's length; therefore, the optical–acoustic length difference contributes 0.50×10^{-6} to the relative uncertainty $u_r(k_B)$.

As in [8], we used dimensional metrology to determine the radius a of the cavity and we confirmed it by measuring the ratios of the frequency of the $(0\,1\,0)$ radial acoustic mode to those of the $(l\,0\,0)$ longitudinal modes. The uncertainty $u_r(a)$ makes a negligible contribution to $u_r(k_B)$.

Table 2 lists the dimensions of the cavity for the three cases. The largest contributor to the uncertainty of the average length of the cavity was 43 nm, which resulted from fitting the shape of the curved end-plates. This uncertainty contributed 1.08×10^{-6} to $u_r(k_B)$. In the future, we will reduce this contribution by using a denser grid of optical length measurements.

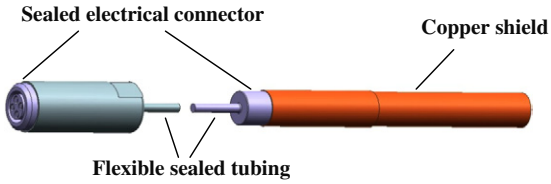

Figure 7. Sketch of the thermometer assembly.

4.3. Temperature measurement

We measured the temperature of the cavity with two 25 Ω standard capsule-type platinum resistance thermometers (Hart 5686-001-B), HS182 and HS192. Each thermometer had an outer diameter of 5.5 mm and a length of 35 mm. Following [5, 6], we enclosed each thermometer within a copper sleeve, as shown in figure 7. These sleeves allowed us to move the thermometers between a triple-point-of-water (TPW) cell and the wells in the resonator's wall without disturbing the thermometers or changing their thermal resistance. The sleeves also protected the thermometers from the hydrostatic pressure during the acoustic measurements. Each sleeve had one sealed end and a length of 100 mm, an outer diameter of 10 mm, an inner diameter of 5.6 mm, and a sensing head 40 mm long. Each thermometer was covered with thermally conducting grease and inserted into the open end of a sleeve. Then, a cap was screwed onto the sleeve to hold the thermometer against the inner wall and the blind end of the sleeve. The four leads from each thermometer passed through a thin stainless-steel tube (inner diameter 2.13 mm and length 500 mm) to welds at a sealed feed-through. After connecting the leads, assembling the sleeve, the tube and the feed-through, the assembly was evacuated and purged with pure argon gas five times. Finally, the assembly was filled with pure argon gas to 110 kPa and sealed with a valve.

The TPW cell used for the calibration of the two thermometers was compared with NIM's national reference cell. The difference was no larger than 0.03 mK and it contributed 0.11×10^{-6} to $u_r(k_B)$. The T_{TPW} of the reference cell was corrected for the effect of isotopes. A bilateral comparison conducted in 2011 demonstrated that the T_{TPW} of the reference cell differed from the average value of two of INRIM's transport cells by 0.01 mK. A bilateral comparison conducted in 2010 demonstrated that the T_{TPW} of the reference cell differed from PTB's reference cell by 0.03 mK. After considering the CCT-K7 and the EURAMET.T-K7 Key Comparison of Water Triple Point Cells, we conservatively estimate a type-B uncertainty of 0.05 mK for NIM's TPW reference cell. This uncertainty contributed a type-B relative uncertainty of 0.18×10^{-6} to $u_r(k_B)$.

The two thermometers were calibrated in the TPW cell before being installed in the wells in the resonator. Table 3 lists the initial calibration data for HS182 and HS192. We

Table 3. Calibration of thermometers. All resistances are in ohms.

No	1 mA	$\sqrt{2}$ mA	1 mA	0 mA
		HS 182		
		Initial calibration		
1	25.069 796	25.069 827	25.069 795	25.069 764
2	25.069 792	25.069 824	25.069 792	25.069 760
3	25.069 790	25.069 822	25.069 790	25.069 758
4	25.069 792	25.069 823	25.069 791	25.069 760
5	25.069 792	25.069 824	25.069 792	25.069 760
6	25.069 792	25.069 824	25.069 791	25.069 760
7	25.069 792	25.069 824	25.069 792	25.069 760
		Final calibration		
1	25.069 794	25.069 826	25.069 794	25.069 762
2	25.069 790	25.069 821	25.069 789	25.069 758
3	25.069 790	25.069 822	25.069 790	25.069 758
4	25.069 792	25.069 824	25.069 791	25.069 760
5	25.069 790	25.069 823	25.069 790	25.069 758
		HS 192		
		Initial calibration		
1	25.428 991 92	25.429 031 96	25.428 991 67	25.428 9516
2	25.429 000 04	25.429 040 34	25.428 999 17	25.428 9589
3	25.428 999 97	25.429 040 39	25.428 999 91	25.428 9595
4	25.428 994 41	25.429 033 99	25.428 993 41	25.428 9538
5	25.428 993 56	25.429 033 54	25.428 993 08	25.428 9531
6	25.428 9941	25.429 033 28	25.428 993 77	25.428 9546

checked for effects from the connection of the cable leading from the feed-through for each thermometer to the resistance bridge by plugging in and unplugging each connector during each calibration. After each calibration, the thermometer was removed from the TPW cell and stored at room temperature. The initial calibration for HS182 at 0 mA had a repeatability of 0.019 mK. HS182 was re-calibrated after finishing all the acoustic measurements. We call this re-calibration the 'post-calibration'. Table 3 lists the post-calibration data for HS182. The post-calibration had a repeatability of 0.018 mK. The pre- and post-calibration were separated by 10 months. The difference between the two averages of the pre- and post-calibrations was 0.011 mK; it is a measure of the long-term stability of the thermometers and it contributed 0.04×10^{-6} to $u_r(k_B)$.

The initial calibration of HS192 had a repeatability of 0.03 mK (the standard deviation of repeated calibration measurements) and a maximum temperature difference (among those repeated measurements) of 0.08 mK. The long-term stability of HS192 was comparable to the long-term stability of HS182, which we discuss below.

The TPW cell was made at the NIM. For this cell, the calculated hydrostatic pressure effect was 0.182 mK; both thermometer calibrations were corrected for this. During the calibrations, the axial temperature gradient was measured by pulling each thermometer along the well of the TPW cell. The measured axial gradients were $-1.12\,\mathrm{mK\,m^{-1}}$ or less. (A gradient of $-0.73\,\mathrm{mK\,m^{-1}}$ is expected [30].) The larger-than-expected gradient biased the temperature calibration by up to 0.097 mK, which contributes a fractional uncertainty of 0.36×10^{-6} to $u_r(k_B)$.

As shown in figure 4, the thermometers were inserted into wells drilled part-way through the wall of the resonator. HS192 was inserted into the well at the top of the resonator. The insertion depth was more than the sensing length (40 mm) of the thermometers. HS182 and HS192 were read alternately during the scanning of every acoustic resonance. Each thermometer was read at 1 mA and $\sqrt{2}$ mA and the result was extrapolated to 0 mA. A complete acoustic measurement lasted for around 5 h. The two thermometers were alternately read parallel to the acoustic measurement. Therefore, the temperature drift of the cylinder shell was monitored. This drift slightly varied with individual test run. We observed that the drifts were bounded within the minimum of ∼0.2 mK and the maximum of ∼1.2 mK. Usually, the differences between the average readings of two thermometers were within ±0.1 mK. (At only one point they differed by 0.2 mK and at two points by slightly more than 0.1 mK.) These small temperature differences are consistent with a negligible temperature gradient along the resonator and with stable performance of both thermometers. We concluded that the long-term stability of HS192 was as good as the long-term stability of HS182. The standard deviation of the temperature differences was 0.047 mK and it contributed a fractional uncertainty of 0.17×10^{-6} to $u_r(k_B)$.

4.4. Chemical and isotopic composition

For the measurements reported in this paper, we used two grades of pure argon supplied by Air Products Inc.: 'BIP Plus' argon and 'BIP' argon. The 'BIP Plus' argon from one container was used for the measurements of cases I and II. For case III, we used the 'BIP' argon from the same container that we used in our previous measurements [8]. The 'BIP' argon in its original container links the present measurements to the isotopic and the impurity references of the Center for Gas Metrology of the KRISS, one of the world's leading gas analysis laboratories.

According to the manufacturer, 'BIP Plus' and 'BIP' are manufactured using identical processes. The only difference between the two grades is their specification for the concentration of volatile organic compounds (VOCs). Each production 'lot' is analysed and if, by chance, the concentration of VOCs is low, the gas is sold as 'BIP Plus' grade. If the VOC analysis is normal, the gas is sold as 'BIP' grade. This distinction implies that the two grades have, at most, only small differences in their relative isotopic abundances for argon and only small differences in their concentrations of the noble gas impurities: He, Ne, Xe and Kr. During the present measurements, we sent samples of 'BIP Plus' and 'BIP' drawn from their original containers to the state Key Laboratory of Petroleum Resource Research, Chinese Academy of Sciences (KLPRR CAS), for new analyses of the relative isotopic abundances. We drew these samples from the manifold downstream of the getter. Two samples of 'BIP Plus' from the same container were labelled samples A and B, and the sample of 'BIP' was labelled sample C. The sampling and naming were blind to the analysing laboratory. Sample C was taken from the original container used for our previous determination of k_B [8], which had also been analysed by the Center for Gas Metrology, KRISS. Samples A, B and C were analysed with the gas chromatography–mass spectrometry (GC–MS) system (MAT271) in KLPRR CAS.

Table 4. Argon isotopic analysis.

	^{40}Ar/^{36}Ar	^{38}Ar/^{36}Ar	Molar mass[a] of argon/ g mol^{-1}
Sample C, BIP	299.52±0.16	0.1894±0.0005	39.947 839
Sample B, BIP Plus	298.70±0.43	0.1884±0.0007	39.947 806
Sample A, BIP Plus	298.68±0.33	0.1895±0.0006	39.947 798
Sample C, BIP, re-measured	299.60±0.27	0.1890±0.0003	39.947 846
Sample A, BIP Plus, re-measured	299.05±0.28	0.1886±0.0008	39.947 822
Sample B, BIP Plus, re-measured	298.87±0.36	0.1882±0.0009	39.947 815

[a] Molar masses of ^{36}Ar, ^{38}Ar and ^{40}Ar are from CODATA 2010 [19].

Both KRISS and KLPRR CAS analysed sample C. Therefore, sample C links the isotopic abundance reference standards of both laboratories, assuming that the relative abundances of the argon isotopes did not change during storage. At KLPRR CAS, the samples were analysed in the order 'C–B–A–C–A–B' to minimize bias. Each measurement was repeated more than five times. In table 4, we list the results of the KLPRR CAS analyses based on the KRISS's reference standards.

The two analyses of sample C resulted in a relative difference of 0.16×10^{-6} in the molecular mass of argon, M. This difference was included in the uncertainty budget for the molar mass of the sample of the 'BIP Plus' gas; it is a measure of the imperfection of the linkage to KRISS's reference standards. Table 4 shows that the repeatability of M for samples A and B was 0.30×10^{-6} and 0.12×10^{-6}, respectively. The relative difference of M between A and B was $(0.02 \pm 0.65) \times 10^{-6}$, where the uncertainty here is the root of the sum of the squares of the repeatability. These differences were also included in the uncertainty budget for M of 'BIP Plus'.

The isotopic abundance ratios ^{40}Ar/^{36}Ar for samples A and B are slightly smaller than that for sample C. The ^{38}Ar/^{36}Ar ratios for samples A, B and C are identical, within the uncertainty of the measurements. The value of M of sample C is larger than the average M of samples A and B by a fraction of 0.81×10^{-6}. For re-determining k_B, we averaged the values of M of samples A and B in table 4. The relative standard uncertainty of the average of samples A and B is $u_r(M) = 0.77 \times 10^{-6}$. This uncertainty is entered into table 8 and it includes the uncertainty of the analysis by KRISS for 'BIP' and the repeatability of the analysis by KLPRR CAS for samples A, B and C.

Our results for k_B are independent of previously published values of M. However, the isotopic composition of commercially prepared argon has been widely discussed by others, who deduced values of k_B from measurements of the speed of sound in argon. See figure 8 and [3–6, 8, 31–34]. In this context, we note that our results for M and $u_r(M)$ are in good agreement with most of the previously published values.

For this work (section 3), we used an SAES Model GC50 getter to purify argon. (Other groups have used the same model [3, 5, 6].) According to the manufacturer, this getter

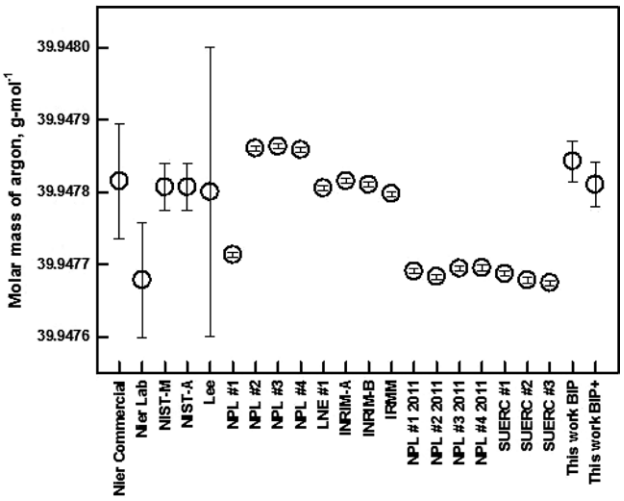

Figure 8. Comparison of argon molar masses. The data sources are Nier [34]; NIST-M and NIST-A [3]; Lee [32]; NPL #1 through IRMM [31]; NPL #1 2011 through SUERC #3 [33]. Note: [33] did not calibrate their spectrometer with argon samples of well-known isotopic abundances; therefore, their results are relative.

Table 5. KRISS analysis of BIP argon.

Gas	Upper bound	u (upper bound)
He	$<1.6 \times 10^{-6}$	0.9×10^{-6}
Ne	$<1.1 \times 10^{-6}$	0.6×10^{-6}
Kr	$<0.3 \times 10^{-6}$	0.2×10^{-6}
Xe	$<0.5 \times 10^{-6}$	0.3×10^{-6}

reduces the concentrations of H_2O, CO, CO_2, O_2, H_2, N_2, CH_4 and other hydrocarbons in argon gas to less than 0.01 parts per million by volume. Therefore, these impurities made negligible contributions to M_{Ar} and its uncertainty.

The upper concentration bounds of noble gas impurities (table 5) contributed a relative uncertainty of 1.12×10^{-6} to $u_r(k_B)$. To summarize, we used the value $M = 39.947\,810(10)$ g mol^{-1} for cases I and II and the value $M = 39.947\,843(5)$ g mol^{-1} for case III.

4.5. Frequency measurements

4.5.1. Spectrum of the evacuated resonator. Figure 9 compares the spectrum of the voltage amplitude at the detector when the cavity was evacuated to the spectrum when the cavity was filled with argon at 150 kPa and 273.16 K. (These spectra were taken before we exchanged the end-plates following the case I measurements.) The vacuum spectrum shows many narrow features, particularly above 7 kHz; however, we did not detect problems connected with these features. Perhaps these features were damped when the cavity was filled with gas. Even if they were not damped, the gas resonances in the cavity generated signals that were a factor of 50 larger than the features in the vacuum spectrum.

4.5.2. Determining measured resonance frequencies f_N and half-widths g_N. We used the method described in [8] to determine the measured values of the resonance frequencies f_N and the half-widths g_N. We stepped the drive transducer

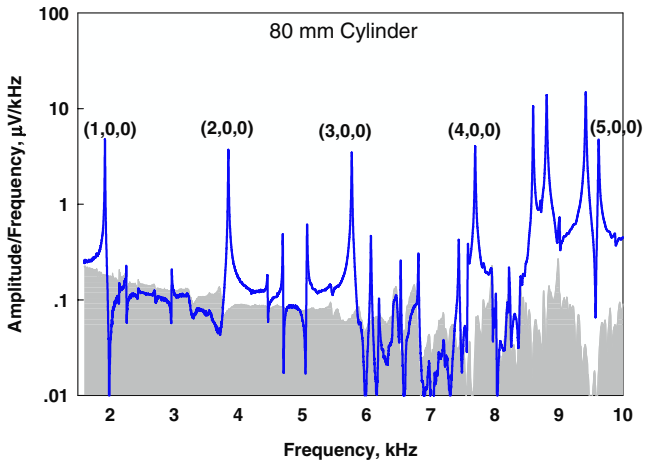

Figure 9. Spectrum (amplitude) of the detected signal when the resonator was evacuated (grey band) and when the resonator was filled with argon at 150 kPa and 273.16 K.

through 13 synthesized, discrete frequencies in increments of $g_N/3$ starting at $f_N - 2g_N$ and ending at $f_N + 2g_N$. Then we changed the step size to $-g_N/3$ and stepped back to $f_N - 2g_N$. After finishing the up and down frequency sweeps for each mode, we waited 1200 s for the heat generated by the drive PZT to dissipate before making additional measurements. At each frequency, the complex voltage $V \equiv u + \mathrm{i}v$ generated by the detector transducer was measured by a Stanford SR830 lock-in amplifier. The 26 frequencies and complex voltages were fitted by the resonance function

$$V = \frac{\mathrm{i}fA}{f^2 - (f_N + \mathrm{i}g_N)^2} + B + C(f - \tilde{f}) + D(f - \tilde{f})^2, \quad (6)$$

where A, B, C and D are complex constants; $F_N = f_N + \mathrm{i}g_N$ is the complex resonance frequency of mode N under study. The parameter $\tilde{f}$ has no physical significance; it is needed only for numerical stability; therefore, we usually set it equal to the average frequency. The parameters B and C account for the effects of possible cross-talk and the 'tails' of the modes other than N. In all the fits, the term $D(f - \tilde{f})^2$ in equation (4) was not significant. The changes in the fitted value of F_N were insignificant when we reduced the span of the data to $f_N \pm 1.7g_N$ by deleting the measurements at the highest and lowest frequencies. For the reduced data span, $f_N \pm 1.7g_N$, the term $C(f - \tilde{f})$ was not significant.

The contributions to g_N in equation (4) from the thermal and viscous boundary layers vary as $f^{-1/2}$. This phenomenon generates a small asymmetry in the shape of the resonance. To account for this, we used the correction

$$\Delta f_N = f_{\mathrm{meas}} - f_N \approx -f_N/(8Q_N^2) \quad (7)$$

to obtain the measured resonance frequency f_{meas}. In this work, the smallest value of Q was 350 for the mode (2 0 0) at 50 kPa, where $\Delta f_N = 1.0 \times 10^{-6}$ in equation (7) and the fractional correction to k_{B} is twice as large.

4.5.3. Excess half-widths. The calculated values of the half-widths account for five effects:

(1) the first-order contribution $g_{\mathrm{v}}^{(1)}/f$ due to the viscous boundary layer using equation (7) from [8],

(2) the first-order contribution $g_{\mathrm{th}}^{(1)}/f$ due to the thermal boundary layer including penetration of the thermal wave into the steel side-wall and the quartz end-plates of the cavity using equation (11) from [8],

(3) thermal and viscous contributions g_{bulk}/f due to the volume losses using equation (12) from [8],

(4) the fill duct using a modified version of the waveguide model presented in [22] (in this model, the values of g_{duct}/f range from 27×10^{-6} for the (2 0 0) mode to 7×10^{-6} for the (5 0 0) mode and have a weak pressure dependence),

(5) the second-order correction to the half-widths from the thermal and viscous boundary layers using

$$\frac{g_{l,\mathrm{surf}}^{(2)}}{f_l^{(0)}} = -\left(\frac{\delta_T}{R}\right)^2 \left[\frac{1}{4}(2\sqrt{Pr} + 3\gamma - 2)(\gamma - 1) + (2\sqrt{Pr} + 3\gamma - 3)(\sqrt{Pr} + \gamma - 1)\frac{R}{L} + 2(\gamma - 1)^2\frac{R^2}{L^2}\right]^2 \quad (8)$$

from [35].

Equation (8) always decreases the calculated half-widths and does not affect the resonance frequencies, as in the case of the spherical cavity [36]. In this work, the values of $g^{(2)}/f$ range from -6.6×10^{-6} to -0.25×10^{-6}; the most negative value occurs for the (2 0 0) mode at 50 kPa and the least negative value occurs for the (5 0 0) mode at 550 kPa. (Because the values of $g^{(2)}/f$ are so small, equation (8) ignores the penetration of the thermal wave into walls of the cavity.)

For calculating $g^{(1)}/f$ and $g^{(2)}/f$, we used the zero-density values $\eta_{\mathrm{Ar}} = (20.9448 \pm 0.0050)$ μPa s and $\lambda_{\mathrm{Ar}} = (16.3673 \pm 0.0039) \times 10^{-3}$ W m^{-1} K^{-1} for the viscosity and thermal conductivity of argon at T_{TPW}. We obtained this value of η_{Ar} by combining the value $\eta_{\mathrm{He}} = (18.677\,47 \pm 0.000\,18)$ μPa s calculated by [37] with the ratio $\eta_{\mathrm{Ar}}/\eta_{\mathrm{He}} = (1.121\,39 \pm 0.000\,27)$ measured in [38]. We obtained the value of λ_{Ar} using the relation $\lambda_{\mathrm{Ar}} = C_p\eta_{\mathrm{Ar}}/(PrM)$, with the value $Pr = (0.665\,851 \pm 0.000\,027)$ for the Prandtl number calculated by [37]. In this work, we used the same expressions for the pressure dependence of the thermal conductivity and the viscosity as we did in [8]. The uncertainties $u(\eta_{\mathrm{Ar}})$ and $u(\lambda_{\mathrm{Ar}})$ contribute less than 0.5×10^{-6} to $u(k_{\mathrm{B}})$.

The upper panel of figure 10 displays the excess half-widths $\Delta g \equiv g_{\mathrm{meas}} - g_{\mathrm{calc}}$ of the acoustic resonances multiplied by $2 \times 10^{-6}/f_{\mathrm{meas}}$, where f_{meas} are the measured frequencies and where g_{calc} is calculated without adjustable parameters. (The factor of 2×10^{-6} is convenient for comparing $\Delta g/f_{\mathrm{meas}}$ with the components of the uncertainty budget for the determination of k_{B}.) At the higher pressures, the present values of $\Delta g/f_{\mathrm{meas}}$ approach straight lines with mode-dependent slopes and intercepts near zero. This trend has been reported by us [8] and by many others and is usually attributed to dissipation in the resonator's elastic response to the oscillating acoustic pressure within it. At low pressures, the present values of $\Delta g/f_{\mathrm{meas}}$ increase approximately as (pressure)$^{-1}$ with only a weak mode dependence. Both of these

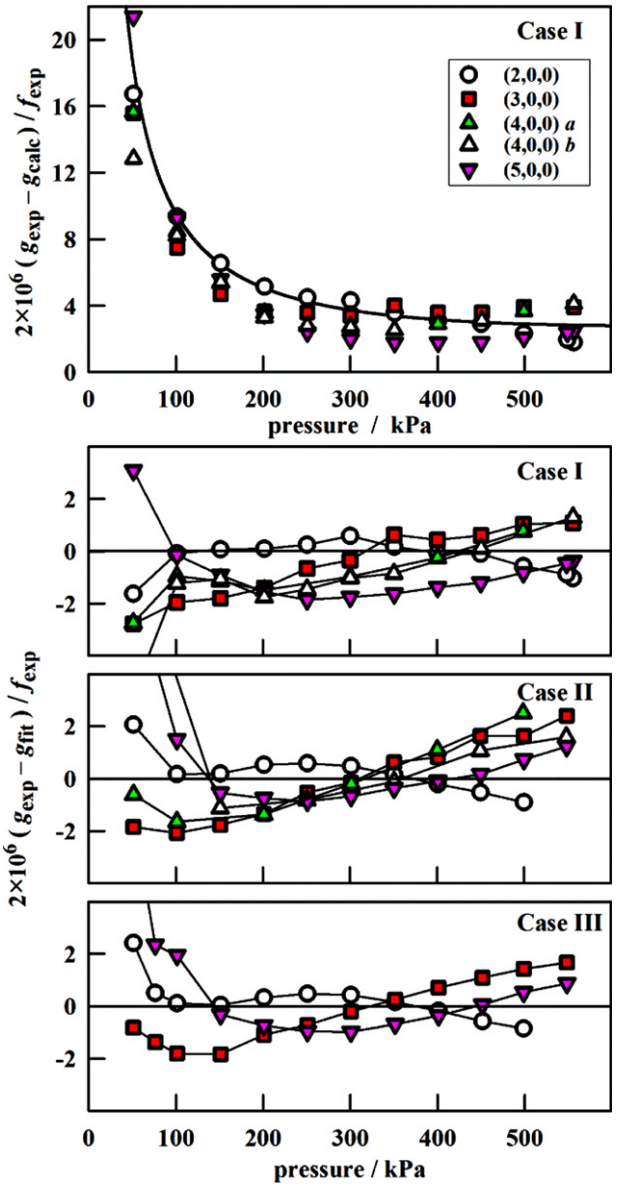

Figure 10. Top: pressure dependence of the excess half-widths multiplied by $2 \times 10^6/f_{\rm exp}$ for case I. The solid curve is the function $0.5683(p/550\,{\rm kPa}) + 0.8496(p/550\,{\rm kPa})^{-1}$. The lower three panels show the deviations of the measured half-widths from the function in the top panel.

trends are represented by the function $0.5683 \times (p/550\,{\rm kPa}) + 0.8496(p/550\,{\rm kPa})^{-1}$ which is plotted as a solid curve in the upper panel of figure 10.

To the best of our knowledge, the increase in $\Delta g/f_{\rm meas}$ at low pressures has not been reported before and we have no explanation for it; however, we are actively studying it. (We are considering dissipation within the transducers and in the sound-absorbing material behind them.) As discussed below, any p^{-1} dependence of the measured frequencies $f_{\rm meas}$ would be absorbed in the term $A_{-1}p^{-1}$ used when fitting $f_{\rm meas}(p)$. Our values of A_{-1} (section 4.6.3) are consistent with accommodation coefficients near unity. Therefore, the low-pressure anomaly in $\Delta g/f_{\rm meas}$ does not appear to affect our values of $k_{\rm B}$.

4.5.4. Corrections to the resonance frequency measurements. The measured resonance frequencies $f_{\rm meas}(T_i, p_i)$ were corrected for four effects:

(1) the viscous boundary layer including the viscous accommodation length $l_{\rm v}$ using equation (4) from [8],

(2) the thermal boundary layer accounting for penetration of the thermal wave into the metal wall and quartz end-plates and including the thermal accommodation length $l_{\rm th}$ (for this effect, we used equation (8) from [8]),

(3) the fill duct, using a modified version of the waveguide model presented in [22] (the waveguide model predicts the fractional correction to $f_{\rm meas}$ is less than 0.6×10^{-6}),

(4) the motion of the shell generated by the oscillating acoustic pressure in the argon. The shell's response was calculated using equations (13) and (20) from [8] with the compliance parameters $G^*_{i,n} \equiv 10^{12}\,{\rm J\,m^{-3}}\ G_{i,n}$ for (i) radial motion $G^*_{1,2} = 0.614$, $G^*_{1,3} = 0.144$, $G^*_{1,4} = 0.0602$ and $G^*_{1,5} = 0.0211$ with $f_{{\rm sh},1} = 25\,308$ Hz for $l = 2, 4$ and $f_{{\rm sh},1} = 64\,562$ Hz for $l = 3, 5$; (ii) axial motion $G^*_2 = 3.22$ with $f_{{\rm sh},2} = 166\,61$ Hz; (iii) end-plate bending (clamped boundary) $G^*_3 = 52.4$ with $f_{{\rm sh},3} = 140\,70$ Hz; (iv) PZT transducer + diaphragm bending $G^*_{\rm dm} = 13.02$ with $f_{\rm dm} = 156\,14$ Hz; equation (14) in [8] was used to estimate the frequency shift due to recoil assuming the resonator is a free rigid body with mass $M_{\rm Res} = 10.442$ kg.

Corrections (2) and (3) in the preceding paragraph require values for the accommodation lengths $l_{\rm v}$ and $l_{\rm th}$; we calculated these corrections assuming $h_{\rm v} = 1$ and $h_{\rm th} = 1$. These accommodation corrections increase the measured frequencies by a fraction $[2(\gamma-1)l_{\rm th} + l_{\rm v}]/a = 11 \times 10^{-6}(50\,{\rm kPa}/p)$ where the simple functional form and numerical value apply to the $(l\,0\,0)$ modes used in this work. To account for the possibility that $h_{\rm v} \neq 1$ and $h_{\rm th} \neq 1$, we included the term $A_{-1}p^{-1}$ in equation (10), the function that we used to fit c^2 as a function of pressure. For cases I and II, the best-fit values of A_{-1} were indistinguishable from zero (table 6) and for case III the term $A_{-1}p^{-1}$ contributed the fraction $(2.2 \pm 1.3) \times 10^{-6}$ to c^2 at our lowest pressure 50 kPa.

The corrections do not account for dissipation due to the transducers or the sound-absorbing material placed behind the transducers.

The multiple corrected frequencies, $f_{\rm corrected}(T_i, p_i)$, for each mode near each target pressure were adjusted to $f_{\rm corrected}(T_{\rm TPW}, \langle p\rangle)$ where $\langle p\rangle$ is the average target pressure. These adjustments used the relation

$$\frac{f_{\rm corrected}(T_{\rm TPW}, \langle p\rangle)}{f_{\rm corrected}(T_i, p_i)} = 1 + \left(\frac{1}{c^2}\frac{{\rm d}c^2}{{\rm d}p}\right)_p (\langle p\rangle - p_i) + \left(\frac{1}{c^2}\frac{{\rm d}c^2}{{\rm d}T}\right)_T (T_{\rm TPW} - T_i). \quad (9)$$

Finally, we averaged the adjusted corrected frequencies for the same case, mode and target pressure to obtain a single frequency $f_{{\rm exp},l}(p)$ and standard deviation, which we used in the subsequent analysis. We drop the angular brackets with the understanding that p refers to the average pressure $\langle p\rangle$.

Table 6. Fitted parameters and derived quantities. ($\Delta k_B \equiv 10^6(k_B/k_{B,CODATA} - 1)$ with $k_{B,CODATA} = 1.380\,6488(13) \times 10^{-23}$ J K^{-1} from [19].)

Parameter	Unit	Case I	Case II	Case III
$A_{0,2}$	m^2 s^{-2}	94 755.85(13)	94 755.77(13)	94 755.38(13)
$A_{0,3}$	m^2 s^{-2}	94 755.96(10)	94 755.89(14)	94 755.55(10)
$A_{0,4a}$	m^2 s^{-2}	94 756.43(10)	94 756.39(13)	—
$A_{0,4b}$	m^2 s^{-2}	94 756.28(10)	94 756.29(13)	—
$A_{0,5}$	m^2 s^{-2}	94 756.33(10)	94 756.24(14)	94 755.94(10)
$10^4\ A_{1,2}$	m^2 s^{-2} Pa^{-1}	2.2268(40)	2.2490(53)	2.2540(44)
$10^4\ A_{1,3}$	m^2 s^{-2} Pa^{-1}	2.3670(39)	2.4114(52)	2.4138(43)
$10^4\ A_{1,4a}$	m^2 s^{-2} Pa^{-1}	2.2078(38)	2.2154(53)	—
$10^4\ A_{1,4b}$	m^2 s^{-2} Pa^{-1}	2.2044(39)	2.2266(53)	—
$10^4\ A_{1,5}$	m^2 s^{-2} Pa^{-1}	2.3182(39)	2.3703(52)	2.3727(42)
$10^{11}\ A_2$	m^2 s^{-2} Pa^{-2}	5.407(43)	5.300(63)	5.272(51)
$10^{-2}\ A_{-1}$	m^2 s^{-2} Pa	−34	−15	102(59)
χ^2/ν		0.7	0.3	0.3
		Derived quantities		
$10^4\langle A_1\rangle$	m^2 s^{-2} Pa^{-1}	2.265(74)	2.295(90)	2.347(83)
$\langle A_0\rangle$	m^2 s^{-2}	94 756.17(25)	94 756.12(27)	94 755.62(29)
$10^{23}\ \langle k_B\rangle$	J K^{-1}	1.380 6502(37)	1.380 6495(39)	1.380 6434(41)
$\Delta k_{B,2}$		−2.33	−3.11	−6.48
$\Delta k_{B,3}$		−1.19	−1.87	−4.69
$\Delta k_{B,4a}$		3.81	3.35	—
$\Delta k_{B,4b}$		2.22	2.34	—
$\Delta k_{B,5}$		2.74	1.82	−0.55
$\langle\Delta k_B\rangle$		1.0	0.50	−3.9

4.5.5. Fitting acoustic isotherms. The values of $f_{exp,l}$ were multiplied by the cavity's length L and divided by the eigenvalue l to convert them to experimental speeds of sound $c_{exp,l}$. The upper panel in figure 11 displays the differences between the values of $(c_{exp,l})^2$ and those reported in [3]. The differences are nearly linear functions of the pressure with mode-dependent slopes. We attribute these differences to imperfections of our model for the shell's response to the acoustic oscillations. To account for these linear dependences, we fitted the values of $(c_{exp,l})^2 - A_3 p^3$ for cases I and II by the eight-parameter function of pressure p and mode l:

$$(f_{exp,l}L/l)^2 - A_3 p_3 = A_0 + A_{1,l}p + A_2 p^2 + A_{-1}p^{-1}. \quad (10)$$

In equation (10), $A_0 \equiv c_0^2 = \gamma_0 k_B T_{TPW}/m$, A_2 and A_{-1} were mode-independent adjustable parameters; A_3 was fixed at the value 1.45×10^{-18} m^2 s^{-2} Pa^{-3} taken from [39], and $A_{1,l}$ took on the five values $A_{1,2}$, $A_{1,3}$, $A_{1,4a}$, $A_{1,4b}$ and $A_{1,5}$ for modes (2 0 0), (3 0 0), (4 0 0)a, (4 0 0)b and (5 0 0), respectively. For case III, we did not use data from modes (4 0 0)a and (4 0 0)b, and parameters $A_{1,4a}$ and $A_{1,4b}$ were not determined.

The deviations from the eight-parameter fitting function are plotted in the lower three panels of figure 11. As suggested by the dashed lines in figure 11, the deviations from equation (10) are approximately mode-dependent constants (independent of pressure). This implies that the eigenvalues for the modes studied are not exact integers, or equivalently, there are perturbations from a cylindrical shape that are missing from our model for the cavity resonator. To quantify this mode dependence, we fit the same data by the 12-parameter function of the pressure p and mode l:

$$(f_{exp,l}L/l)^2 - A_3 p^3 = A_{0,l} + A_{1,l}p + A_2 p^2 + A_{-1}p^{-1}, \quad (11)$$

where the single parameter A_0 has been replaced by the five parameters $A_{0,2}$, $A_{0,3}$, $A_{0,4a}$, $A_{0,4b}$ and $A_{0,5}$. The results of this final fit of the data by equation (11) are listed in table 6. The deviations of the data from this fit are the deviations of the points in figure 11 from the corresponding dashed lines.

When fitting equations (10) and (11), we weighted each value of $(f_{exp,l}L/l)^2$ by $1/\sigma^2(f^2)$ where $\sigma(f)$ is the standard deviation of the multiple frequencies measured for each mode after being corrected to T_{TPW} and to each target pressure. The values of $\sigma(f^2)$ were represented by the function

$$\sigma(f^2) = f^2\left(s_1 + \frac{s_2}{\tilde{f}\,\tilde{p}} + \frac{s_3}{\tilde{f}\,\tilde{p}^2} + s_4\tilde{f}\,\tilde{p}^2 + s_5\tilde{f}\,\tilde{p}\right), \quad (12)$$

where the coefficients are listed in table 7 and the scaled frequency and pressure are defined by $\tilde{f} \equiv f/(9600\,\text{Hz})$ and $\tilde{p} \equiv p/(550\,\text{kPa})$. With these weights, the values of χ^2 divided by the number of degrees of freedom ν were 0.7, 0.3 and 0.3 for cases I, II and III, respectively. This implies that we overestimated $\sigma^2(f^2)$ by less than a factor of 2.

4.6. Results

Table 6 lists results from fitting all three cases. Figure 5 compares the present values of $A_{1,l}$ and $k_{B,l} = 3mA_{0,l}/(5T_{TWP})$ to reference values. As reference values, we used $A_1 = 2.5202(35) \times 10^{-4}$ m^2 s^{-2} Pa^{-1} from [3] and $k_B = 1.380\,6488(13) \times 10^{-23}$ J mol^{-1} K^{-1} from the CODATA 2010 review [19].

4.6.1. Results for k_B. The upper panel of figure 5 shows the 13 values of k_B determined in this work. They are scattered in a non-random manner about the CODATA 2010 value. First,

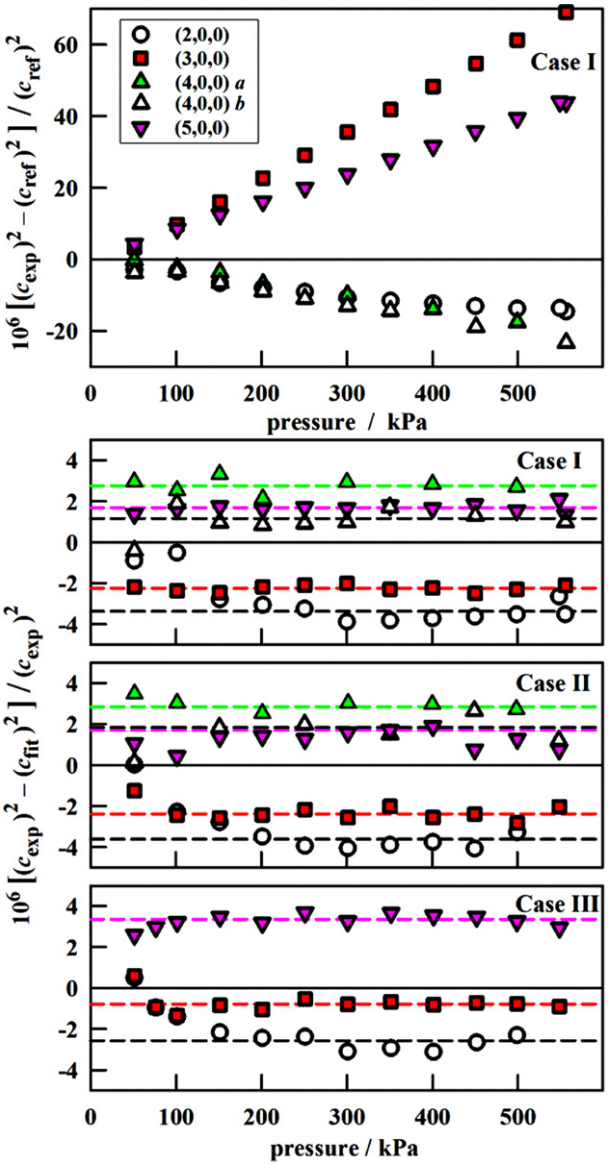

Figure 11. Top: deviations of measured squared speed of sound from the results reported in [3]. The lower three panels display the deviations for each case from weighted fitting of the values of $(c_{\mathrm{exp},l})^2 - A_3 p^3$ to the surface $A_0 + A_{1,l}\,p + A_2 p^2 + A_{-1} p^{-1}$, where the subscript '$l$' identifies the mode-dependent parameter.

we identify the correlations in the data. Then, we compute a particular average value $\langle k_{\mathrm{B}} \rangle$.

We quantify the consistent mode dependence of k_{B} by comparing the standard deviation of the five mode-by-mode differences between cases I and II with the standard deviation of the same ten values of k_{B}. The average of the five differences is $\langle k_{\mathrm{B,case\ II}} - k_{\mathrm{B,case\ I}} \rangle = (-0.54 \pm 0.41) \times 10^{-6} k_{\mathrm{B}}$. In contrast, the average of the same ten values is $\langle k_{\mathrm{B,cases\ I\ and\ II}} \rangle - k_{\mathrm{B,Ref}} = (0.78 \pm 2.60) \times 10^{-6} k_{\mathrm{B}}$ with a standard deviation that is six times larger. We recall that, between cases I and II, the end-plates were interchanged, the length of the cavity decreased by a fraction of 10.0×10^{-6}, and the support of the cavity was changed from nearly free to clamped. Thus, the small standard deviation of mode-by-mode differences is consistent with (1) part-per-million reproducibility of the measurements of temperature and length, (2) reproducible handling of argon during ten runs and (3) apparent values of k_{B} that are independent of the method of supporting the cavity.

Table 7. Coefficients for equation (12) for the uncertainty $\sigma(f^2)$.

	Case I	Case II	Case III
s_1	0.0990	0.5322	0
s_2	0.1165	0	0.1305
s_3	0	0.0166	0
s_4	0	0.4093	0
s_5	0	0	0.4651

Table 8. Uncertainty budget for the re-determination of k_{B}.

Uncertainty source	Reference	$10^6 \times u_{\mathrm{r}}(k_{\mathrm{B}})$
1. Gas temperature measurement	section 4.3	
Thermometer calibration		0.36
Temperature gradient		0.17
TPW realized by the reference cell		0.18
2. Avogadro constant	[19]	0.05
3. Molar mass	section 4.4	
Abundance of noble gas impurities		1.12
Isotopic abundance ratios		0.77
4. Length measurement	section 4.2	
Average cavity length		1.08
Optical–acoustic difference		0.50
Two-colour interferometry		0.58
5. Zero-pressure limit of corrected frequencies	section 4.5	
Boundary layer corrections		0.40
Random error in A_0	table 6	1.2
6. Inconsistency among four modes	section 4.6.1	2.9
Combined uncertainty		3.7

Between cases II and III, we replaced BIP+ argon with BIP argon. The average of the three mode-by-mode differences is $\langle k_{\mathrm{B,case\ III}} - k_{\mathrm{B,case\ II}} \rangle = (-2.85 \pm 0.50) \times 10^{-6} k_{\mathrm{B}}$. We attribute this difference to a real difference between the mole fraction average mass M of the two argon samples. The fractional difference, 2.85×10^{-6}, is 2.1 times the uncertainty $u_{\mathrm{r}}(M)$ of each test gas (section 4.4 and table 8) and it is 1.5 times $2^{1/2} u_{\mathrm{r}}(M)$, the fractional standard uncertainty of the difference between two values of M. This estimate of $u_{\mathrm{r}}(M)$ does not separate out the random and correlated parts of the mass uncertainty; therefore, it may be very large.

Because the values of k_{B} from cases I and II are correlated, both by mode and by argon sample, we treat cases I and II as a single measurement with the result $\langle k_{\mathrm{B,cases\ I\ and\ II}} \rangle - k_{\mathrm{B,Ref}} = 0.78 \times 10^{-6} k_{\mathrm{B}}$. We treated case III as a second measurement; however, the data for the (4 0 0) mode were not usable for case III. Therefore, we used the (2 0 0), (3 0 0) and (5 0 0) modes to calculate the difference between cases {I and II} and case III to obtain the result $\langle k_{\mathrm{B,case\ III}} \rangle - \langle k_{\mathrm{B,cases\ I\ and\ II}} \rangle = (3.25 \pm 0.47) \times 10^{-6} k_{\mathrm{B}}$. The unweighted average of these 'two' measurements is $\langle k_{\mathrm{B}} \rangle_{\mathrm{two}} - k_{\mathrm{B,Ref}} = -0.85 \times 10^{-6} k_{\mathrm{B}}$, which corresponds to $k_{\mathrm{B,this\ work}} = 1.380\,6476 \times 10^{-23}\,\mathrm{J\,K^{-1}}$. This average is our best estimate of k_{B} because it gives equal weight to the data from the BIP+ argon and the BIP argon, and because it recognizes that we used only four independent modes. If we had simply computed the average of all 13 values of k_{B}, we

would have weighted the BIP+ argon data (cases I and II) a factor of 10/3 more heavily than the BIP argon (case III) and obtained the result $\langle k_B \rangle_{13} - k_{B,Ref} = -(0.30 \pm 3.29) \times 10^{-6} k_B$, where the uncertainty is only the standard deviation of the 13 values of k_B.

We quantify the mode-dependent inconsistency among the values of k_B by the standard deviations of the differences between the values of k_B for each case and their mean; they are 2.7×10^{-6}, 2.8×10^{-6} and 3.0×10^{-6}, for cases I, II and III, respectively. (If the values of $A_{0,4a}$ and $A_{0,4b}$ are averaged before computing the standard deviation, the values are 2.7×10^{-6} for case I and 2.9×10^{-6} for case II.) These results are summarized by the entry 'inconsistency among modes' with the value 2.9×10^{-6} in our uncertainty budget in table 8.

4.6.2. Results for the acoustic virial coefficients A_1 and A_2. The lower panel of figure 5 show the 13 values of A_1 determined in this work. (The values of $A_{1,n}$ are listed in table 6.) They are scattered about the reference value $A_1 = 2.5202(35) \times 10^{-4}\ \mathrm{m^2\,s^{-2}\,Pa^{-1}}$ from [3]. The mode-by-mode differences have the averages $\langle A_{1,\text{case II}} - A_{1,\text{case I}} \rangle = (0.030 \pm 0.018) \times 10^{-4}\ \mathrm{m^2\,s^{-2}\,Pa^{-1}}$ and $\langle A_{1,\text{case III}} - A_{1,\text{case II}} \rangle = (0.0033 \pm 0.0015)$. Because A_1 has contributions from both the second acoustic virial coefficient of argon and from the response of the resonator to the gas oscillations, it is not surprising that exchanging the end-plates and changing the support of the resonator changed $\langle A_1 \rangle$. Furthermore, the values of A_1 for the odd modes (3 0 0) and (5 0 0) changed more than the values for the even modes, perhaps because the odd modes tend to move the centre of mass of the resonator while the even modes do not. We did not expect $\langle A_1 \rangle$ to change when we changed argon from BIP+ to BIP. Consistent with this expectation, the gas change was associated with a change in $\langle A_1 \rangle$ that was only 1/10th of the change associated with the support and was barely significant.

Fitting equation (11) yielded the result $\langle A_2 \rangle = (5.326 \pm 0.071) \times 10^{-11}\ \mathrm{m^2\,s^{-2}\,Pa^{-2}}$ which agrees, within combined uncertainties, with the value $(5.321 \pm 0.062) \times 10^{-11}\ \mathrm{m^2\,s^{-2}\,Pa^{-2}}$ reported in [3].

4.6.3. Results for A_{-1} and the accommodation coefficients h. For cases I and II, the best-fit values of A_{-1} in table 6 are zero within the uncertainty of the fit. The value zero is equivalent to a combined accommodation coefficient $h = 1$, assuming that the thermal and the viscous accommodation lengths l_v and l_{th} are both multiplied by the factor $(2-h)/h$. Determining separate values for h_v and h_{th} would require studying both longitudinal and non-longitudinal acoustic modes; this is not necessary to determine k_B with the present uncertainties. For case III, the value of A_{-1} is equivalent to a combined accommodation coefficient $h = 0.68 \pm 0.17$. Values of h_{th} close to 1 have been reported by other groups that measured k_B using acoustic resonators [40].

4.7. Uncertainty budget

Our determination of k_B is connected to the quantities that we measured (frequencies f, length L, temperature T, pressure p), the calculated eigenvalues l and frequency perturbations Δf, the fundamental constant N_A, and to quantities measured by others (A_3, M). Therefore, the uncertainty $u_r(k_B)$ of the value means k_B has contributions from the uncertainties, $u_r(f_l), u_r(M), u_r(T), u_r(L^2)$, as well a contribution from fitting the frequencies in each run to determine A_0. Table 8 lists these contributions to $u_r(k_B)$ and refers to the sources of the uncertainty estimates.

By far the largest contribution to $u_r(k_B)$ is the inconsistency among the modes. This suggests that our cavity differs from a perfect cylinder in ways that we have not modelled. Although we do not know the origin of this inconsistency, we have treated it as a random effect for estimating uncertainties.

The second largest contribution to $u_r(k_B)$ results from the random uncertainty of the values of A_0 generated by fitting the data on each isotherm. The third largest contribution to $u_r(k_B)$ resulted from the uncertainty of the molar mass of the argon samples. This uncertainty contribution had two parts. The larger of the two resulted from the upper bounds to the concentrations of noble gas impurities provided by the manufacturer. The smaller of these two contributions resulted from the analysis of the relative isotopic abundances.

The root sum of the squares of all the contributions to $u_r(k_B)$ is 3.7×10^{-6} and this is our estimate of $u_r(k_B)$.

5. Discussion

We have re-determined k_B using very different techniques from those that led to the CODATA 2010 value of k_B. Our result differs from this reference by a fraction $(-0.9 \pm 3.7) \times 10^{-6}$. Our result is probably the most accurate value of the speed of sound ever measured with a cylindrical resonator.

The present frequency measurements had a higher signal-to-noise ratio than our previous work and this enabled us to detect a low-pressure anomaly in half-width results. We are actively investigating possible sources of this anomaly. In this work, we reduced the dispersion among the modes; however, this is still a major source of uncertainty. The dispersion indicates that our model for the geometry of the cavity (i.e. its dimensions, including the fill duct and the joints between the end-plates and the sides of the cavity) can be improved.

In [21] we proposed transferring end-plates from one fixed-length cavity resonator to a second, twice-as-long, cavity resonator and to determine k_B by comparing modes of the two cavities at nearly the same frequency. The feasibility of measuring k_B in this way is supported by our observation that values of k_B from cases I and II are nearly identical. If the inconsistency among the modes results from some stable property of the end-plates or some repeatable property of the joint between the end-plates and the cylinder, the two-cavity scheme will reduce the uncertainty of k_B.

In this work we measured the difference between the speed of sound in two different samples of argon using four acoustic modes. The relative standard deviation of the differences in c_0^2 was 0.47×10^{-6}. This demonstrates the feasibility of using a sample of isotopically enriched ^{40}Ar as a mass standard to determine the mass of working gases such as those in particular

cylinders of 'BIP' and 'BIP+'. As shown in [3], this will reduce the uncertainty of M, particularly if tighter upper bounds can be placed on the concentrations of the noble gas impurities in argon.

Acknowledgments

We thank Dr Roberto Gavioso, Dr Laurent Pitre and Dr Michael de Podesta for their many suggestions and continuing interest in our work. We are grateful to Dr LiWu Li of Key Laboratory of Petroleum Resource Research, Chinese Academy of Sciences (KLPRR CAS), for the isotopic analysis of our argon samples. This work was supported by the National Natural Science Foundation of China (Nos 50906076, 51106143 and 51076074).

References

[1] Mills I M, Mohr P J, Quinn T J, Taylor B N and Williams E R 2006 Redefinition of the kilogram, ampere, kelvin and mole: a proposed approach to implementing CIPM recommendation 1 (CI-2005) *Metrologia* **43** 227–46

[2] Colclough A R, Quinn T J and Chandler T R D 1979 An acoustic redetermination of the gas constant *Proc. R. Soc. Lond.* A **368** 125–39

[3] Moldover M R, Trusler J P M, Edwards T J, Mehl J B and Davis R S 1988 Measurement of the universal gas constant R using a spherical acoustic resonator *J. Res. Natl Bur. Stand.* **93** 85–144

[4] Pitre L, Sparasci F, Truong D, Guillou A, Risegari L and Himbert M E 2011 Measurement of the Boltzmann constant k_B using a quasi-spherical acoustic resonator *Int. J. Thermophys.* **32** 1825–86

[5] Sutton G, Underwood R, Pitre L, de Podesta M and Valkiers S 2010 Acoustic resonator experiments at the triple point of water: first results for the Boltzmann constant and remaining challenges *Int. J. Thermophys.* **31** 1310–46

[6] Gavioso R M, Benedetto G, Albo P A G, Ripa D M, Merlone A, Guianvarc'h C, Moro F and Cuccaro R 2010 A determination of the Boltzmann constant from speed of sound measurements in helium at a single thermodynamic state *Metrologia* **47** 387–409

[7] Pitre L, Guianvarc'h C, Sparasci F, Guillou A, Truong D, Hermier Y and Himbert M E 2009 An improved acoustic method for the determination of the Boltzmann constant at LNE-INM/CNAM *C. R. Phys.* **10** 835–48

[8] Zhang J T, Lin H, Feng X J, Sun J P, Gillis K A, Moldover M R and Duan Y Y 2011 Progress toward redetermining the Boltzmann constant with a fixed-path-length cylindrical resonator *Int. J. Thermophys.* **32** 1297–331

[9] Colclough A R 1979 Low frequency acoustic thermometry in the range 4.2–20 K with implications for the value of the gas constant *Proc. R. Soc. Lond.* A **365** 349–71

[10] Moldover M R, Boyes S J, Meyer C W and Goodwin A R H 1999 Thermodynamic temperatures of the triple points of mercury and gallium and in the interval 217 K to 303 K *J. Res. Natl Inst. Stand. Technol.* **104** 11–46

[11] Benedetto G, Gavioso R M, Spagnolo R, Marcarino P and Merlone A 2004 Acoustic measurements of the thermodynamic temperature between the triple point of mercury and 380 K *Metrologia* **41** 74–98

[12] Pitre L, Moldover M R and Tew W L 2006 Acoustic thermometry: new results from 273 K to 77 K and progress towards 4 K *Metrologia* **43** 142–62

[13] Ripple D C, Strouse G F and Moldover M R 2007 Acoustic thermometry results from 271 K to 552 K *Int. J. Thermophys.* **28** 1789–99

[14] Fischer J, Podesta M, Hill K D, Moldover M, Pitre L, Rusby R, Steur P, Tamura O, White R and Wolber L 2011 Present estimates of the differences between thermodynamic temperatures and the ITS-90 *Int. J. Thermophys.* **32** 12–27

[15] Strouse G F, Murdock W E, Ripple D C and Schooley J F 2012 NIST acoustic thermometer results above 550 K *9th Int. Temperature Symp. (Los Angeles, CA, 19–23 March 2012)*

[16] Andrea B *et al* 2011 Determination of the Avogadro constant by counting the atoms in a ^{28}Si crystal *Phys. Rev. Lett.* **106** 030801

[17] de Podesta M, Underwood R, Sutton G, Morantz P, Harris P, Mark D F, Stuart F M, Vargha G and Machin G 2013 A low-uncertainty measurement of the Boltzmann constant *Metrologia* **50** 354–76

[18] Zhang J T, Lin H and Feng X J 2012 An insight to the redetermination of the Boltzmann constant by fixed path cylindrical cavities *9th Int. Temperature Symp. (Los Angeles, CA, 19–23 March 2012)*

[19] Mohr P J, Taylor B N and Newell D B 2012 CODATA recommended values of the fundamental physical constants *Rev. Mod. Phys.* **84** 1527–605

[20] Lin H, Gillis K A and Zhang J T 2010 Characterization of piezoelectric ceramic transducer for accurate speed-of-sound measurement *Int. J. Thermophys.* **31** 1234–47

[21] Zhang J T, Lin H, Sun J P, Feng X J, Gillis K A and Moldover M R 2010 Cylindrical acoustic resonator for the re-determination of the Boltzmann constant *Int. J. Thermophys.* **31** 1273–93

[22] Gillis K A, Lin H and Moldover M R 2009 Perturbations from ducts on the modes of acoustic thermometers *J. Res. Natl Inst. Stand. Technol.* **114** 263–85

[23] Trusler, J P M 1991 *Physical Acoustics and Metrology of Fluids* (Bristol: Adam Hilger) pp 72–4

[24] Peck E R and Fisher D J 1964 Dispersion of argon *J. Opt. Soc. Am.* **54** 1362–4

[25] Montixi G, Occelli R and Coulon R 1980 Réfractivité de l'argon dans le spectre visible en fonction de la pression *J. Opt. (Paris)* **11** 331–5

[26] Zhang J, Lu Z H, Menegozzi B and Wang L J 2006 Application of frequency combs in the measurement of the refractive index of air *Rev. Sci. Instrum.* **77** 083104

[27] Zhang J, Lu Z H and Wang L J 2008 Precision refractive index measurements of air, N_2, O_2, Ar, and CO_2 with a frequency comb *Appl. Opt.* **47** 3143–51

[28] Clergent Y, Durou C and Laurens M 1999 Refractive index variations for argon, nitrogen, and carbon dioxide at 632.8 nm (He–Ne laser light) in the range 288.15 K $\leqslant T \leqslant$ 323.15 K, 0 $< p <$ 110 kPa *J. Chem. Eng. Data* **44** 197–9

[29] Palik E D (ed) 1985 *Handbook of Optical Constants of Solids* (New York: Academic)

[30] Preston-Thomas H, Bloembergen P and Quinn T J 1990 *Supplementary Information for the International Temperature Scale of 1990* (Sèvres: BIPM) p 30

[31] Valkiersa S, Vendelbo D, Berglund M and Podesta M 2010 Preparation of argon primary measurement standards for the calibration of ion current ratios measured in argon *Int. J. Mass Spectrom.* **291** 41–7

[32] Lee J-Y, Marti K, Severinghaus J P, Kawamura K, Yoo H-S, Lee J B and Kim J S 2006 A redetermination of the isotopic abundances of atmospheric Ar *Geochim. Cosmochim. Acta* **70** 4507–12

[33] Mark D F, Stuart F M and de Podesta M 2011 New high-precision measurement of the isotopic composition of atmospheric argon *Geochim. Cosmochim. Acta* **75** 7494–501
[34] Nier A O 1950 A redetermination of the relative abundances of the isotopes of carbon, nitrogen, oxygen, argon, and potassium *Phys. Rev.* **77** 789–93
[35] Gillis K A 2012 Cylindrical resonator eigenvalues to second order including corner, unpublished
[36] Gillis K A 2012 Second-order boundary corrections to the radial acoustic eigenvalues for a spherical cavity *Metrologia* **49** L21–4
[37] Cencek W, Przybytek M, Komasa J, Mehl J B, Jeziorski B and Szalewicz K 2012 Effects of adiabatic, relativistic, and quantum electrodynamics interactions on the pair potential and thermophysical properties of helium *J. Chem. Phys.* **136** 224303
[38] May E F, Moldover M R, Berg R F and Hurly J J 2006 Transport properties of argon at zero density from viscosity-ratio measurements *Metrologia* **43** 247–58
[39] Goodwin A R H 1988 Thermophysical properties from the speed of sound *PhD Thesis* University of London
[40] Moldover M R 2009 Optimizing acoustic measurements of the Boltzmann constant *C. R. Phys.* **10** 815–27